Available online at www.sciencedirect.com

SciVerse ScienceDirect

Acta Materialia 61 (2013) 1809–1819

Acta MATERIALIA

www.elsevier.com/locate/actamat

Fine-structured aluminium products with controllable texture by selective laser melting of pre-alloyed AlSi10Mg powder

Lore Thijs [a,*], Karolien Kempen [b], Jean-Pierre Kruth [b], Jan Van Humbeeck [a]

[a] University of Leuven (KU Leuven), Department of Metallurgy and Materials Engineering, Leuven, Belgium
[b] University of Leuven (KU Leuven), Department of Mechanical Engineering, Leuven, Belgium

Received 1 October 2012; received in revised form 23 November 2012; accepted 30 November 2012
Available online 28 December 2012

Abstract

This study shows that AlSi10Mg parts with an extremely fine microstructure and a controllable texture can be obtained through selective laser melting (SLM). Selective laser melting creates complex functional products by selectively melting powder particles of a powder bed layer after layer using a high-energy laser beam. The high-energy density applied to the material and the additive character of the process result in a unique material structure. To investigate this material structure, cube-shaped SLM parts were made using different scanning strategies and investigated by microscopy, X-ray diffraction and electron backscattered diffraction. The experimental results show that the high thermal gradients occurring during SLM lead to a very fine microstructure with submicron-sized cells. Consequently, the AlSi10Mg SLM products have a high hardness of 127 ± 3 Hv0.5 even without the application of a precipitation hardening treatment. Furthermore, due to the unique solidification conditions and the additive character of the process, a morphological and crystallographic texture is present in the SLM parts. Thanks to the knowledge gathered in this paper on how this texture is formed and how it depends on the process parameters, this texture can be controlled. A strong fibrous $\langle 100 \rangle$ texture can be altered into a weak cube texture along the building and scanning directions when a rotation of 90° of the scanning vectors within or between the layers is applied.

Keywords: Selective laser melting; Al–Si alloys; Laser deposition; Solidification microstructure; Texture

1. Introduction

The present demand for the production of geometrically complex thermal conductive or lightweight structures is driving the research to process aluminium alloys by the current additive manufacturing (AM) techniques. AM techniques are characterized by the direct and layer-wise addition of material to create prototypes or functional products based on three-dimensional computer models. For example, due to the high geometrical freedom allowed by the AM techniques, it is feasible to build complex heat exchange structures with an improved functionality [1]. The AM technique studied in this paper is a powder bed based technique in which a laser beam is used to selectively melt powder material layer by layer. The process is also known as selective laser melting (SLM), direct metal laser sintering (DMLS) or laser beam melting (LBM). More information regarding the process details and applications can be found elsewhere [2].

AlSi10Mg is a widely used casting alloy and is selected in this study for its good weldability and hardenability while maintaining a high thermal conductivity of 113 $W\,m^{-1}\,K^{-1}$ [3] and good corrosion resistance. The good weldability is induced by the near-eutectic composition of Al and Si, which is known to lead to a small solidification range. The addition of small amounts of Mg (0.3–0.5 wt.% Mg) induces hardening of the aluminium alloy by forming Mg_2Si precipitates upon natural or artificial ageing treatments [4].

Previous studies on the feasibility of producing aluminium alloy parts by SLM have shown that the process is more difficult to control than, for example, in the case of processing stainless steels or titanium alloys. This is mainly

* Corresponding author. Tel.: +32 16 321286; fax: +32 16 321270.
E-mail address: lore.thijs@mtm.kuleuven.be (L. Thijs).

1359-6454/$36.00
http://dx.doi.org/10.1016/j.actamat.2012.11.052

attributed to the high reflectivity of the aluminium powder for the laser beam, the high transfer of heat away from the melt pool through the already solidified material and the formation of oxide layers on top of the melt pools [5–7]. However, as previously shown in Refs. [5,7,8], parts with densities exceeding 99% can be produced when using high laser powers of 200 W and above. The microstructure in the as-produced aluminium SLM parts is reported to be a very fine cellular–dendritic solidification structure. The formation of this fine dendritic structure upon laser melting of aluminium was also previously observed in various laser processing techniques like laser surface remelting and laser depositing [9–11]. In laser surface remelting, the formation of this fine structure is used to harden the surface of casted or wrought aluminium products [9,10]. From the research on the laser deposition of an Al–Si alloy by Dinda et al., it is furthermore found that the high-energy density of the laser gives rise to a directional heat transfer and as a result also gives rise to a directional solidification. By repeating the deposition of the beads layer after layer, a ⟨1 0 0⟩ fibre or cube texture depending on the scanning direction is formed [11]. However, the laser deposition process uses higher heat inputs, which results in much larger deposit widths (i.e. 1 mm) compared to the track widths of 100 μm typically formed in SLM. In addition in SLM several scan tracks are placed next to each other in order to fill individual layers in SLM while in laser deposition, usually only walls of single beads are made on top of each other. Furthermore, the thermal gradients are less steep in laser deposition, resulting in a coarser microstructure or even other solidification modes.

In this paper, an attempt is made to go a step further in the previously performed characterization of an aluminium alloy processed with SLM [5–8]. This paper discusses the material structure at the micro- as well as the macroscale. In addition, also the influence of the scanning strategy is taken into account. The scanning strategy, and more particularly the influence of the method of scanning on the produced microstructure and texture, is investigated. The micrographs given in this paper show that changing the scanning strategy also affects the porosity in the parts (i.e. the type and volume percentage of pores). This, however, will not be dealt with in this paper. This paper will focus on the solidification structure and the texture formed in AlSi10Mg SLM parts.

2. Experimental methods and materials

2.1. Production of test specimen by selective laser melting (SLM)

Five times two cubical samples of $15 \times 15 \times 15$ mm^3 were produced on a modified Concept Laser M1 machine [12], which can handle reactive materials in a closely controlled atmosphere. The machine is equipped with a 200 W fibre laser and has a laser beam diameter ($Ø_{99\%}$) of 150 μm. The process parameters to obtain a part with maximal density were optimized in an earlier study [7] and the values are given in Table 1. The same powder batch with spherical particles and a size distribution ranging between 20 μm and 60 μm was used here. The process was carried out under an argon atmosphere with an overpressure of 10–12 mbar and oxygen level of 0.1–0.3%.

The influence of the method of scanning was taken into account by comparing unidirectional scanning with bidirectional scanning. In unidirectional scanning, the laser always starts from the same side of the part, as illustrated in Fig. 1A. In bidirectional scanning, the laser moves in a zigzag way across the surface, as illustrated in Fig. 1B. Also the influence of rotation of the scanning direction between successive layers was investigated. Furthermore, reducing the vector length by dividing the cross-section into islands (so-called "island scanning" strategy) and shifting the position of the scan vectors between the layers were considered. The island size was chosen to be 5×5 mm^2 and a shift of 1 mm of the scanning vectors in both x and y directions was applied. Table 1 gives an overview of the production details of the different samples and their respective relative Archimedes density value and texture index. The scanning strategies for the different samples are also illustrated in Fig. 1. As the rotation of 90° of the long vectors between the layers cannot be set into the Concept Laser machine, each layer was scanned twice for sample C with the same process parameters but rotated over 90°. This approximation can be tolerated since the laser is shining on already solidified material during the second scan and not on powder particles as during the first scan. Therefore, less energy is absorbed and heat is conducted away more quickly. As a result, the size of the second scanned melt pools is smaller than the first scanned ones and part of the first scanned material still remains in the final product.

2.2. Material characterization techniques

The samples were microscopically observed with a light optical microscope, a polarized light optical Axioskop 40 Pol/40 A Pol microscope and a PHILIPS scanning electron microscope XL30 FEG. Keller's etchant was used to reveal the general structure. The different crystallographic orientations could be visualized by the use of polarized light on electrolytically anodized samples in Barker's reagent at 5 V for 5 s. The Vickers microhardness tests were performed on a Leitz–Durimet microhardness tester using a weight of 500 g.

X-ray measurements were performed on a SIEMENS D500 using a Cu tube at 40 kV and 40 mA. The diffraction patterns between a 2θ angle of 23° and 90° were measured using a step size of 0.02° and detection time of 3 s. The pole figures were measured with (1 1 1), (1 0 0), (1 1 0) and (1 1 3) reflections of the (Al) phase. It should be noted that this technique cannot measure the entire pole figure due to defocusing and low gain at angles between the sample and incoming X-rays lower than 10°. Khi was thus measured between 0° and 80° in steps of 5°. At each Khi, a complete circle was measured in steps of 4°. The diffracted

Table 1
Overview of the scanning strategy and scanning parameters of the produced samples and their resulting relative Archimedes density and texture index value.

Sample	A	B	C	D	E
Scanning parameters					
Laser power (W)	200	200	200	200	200
Scanning speed (mm s^{-1})	1400	1400	1400	1400	1400
Hatch spacing (μm)	105	105	105	105	105
Scanning vector bidirectional (Bi) or unidirectional (Uni)	Bi	Uni	Bi	Bi	Bi
Rotation between layers	0°	0°	90°[a]	90°	90°
Islands 5 × 5 mm^2	No	No	No	Yes	Yes
Shift 1 mm	No	No	No	No	Yes
Relative Archimedes density (%) ($\rho_{theor} = 2.68$ g cm^{-3})	99.0	98.9	99.4	98.2	98.7
Texture index (according to Eq. (1))	1.974	1.982	1.266	1.127	1.079

[a] Rotating the long vector strategy 90° is not possible with the current Concept Laser© software. To get an idea of creating melt tracks rotated 90° to the previous scan direction, every layer was scanned twice with the second scanned tracks rotated over 90° to the first scanned ones.

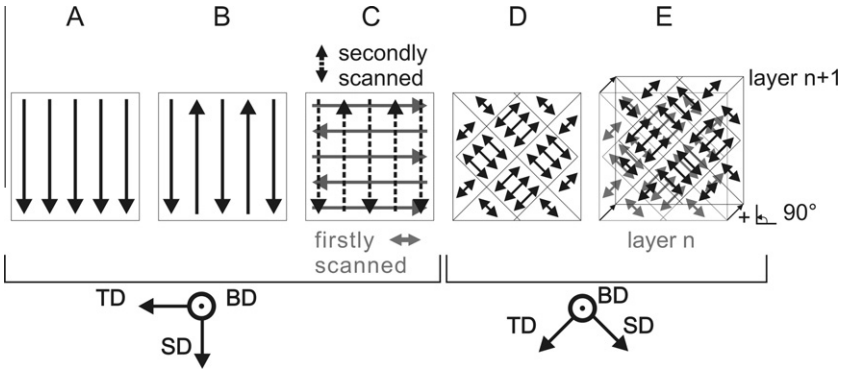

Fig. 1. Overview of the scanning strategy used for the different samples. The building (BD), scanning (SD) and transverse direction (TD) are indicated. Sample A is scanned with long unidirectional vectors; sample B with long bidirectional vectors; sample C is first scanned with long bidirectional vectors in TD and secondly scanned with long bidirectional vectors in SD; sample D is scanned with island strategy with 90° rotation but without shift and sample E is scanned with island strategy with 90° rotation and 1 mm shift between the layers.

beam was recorded during 1 s for each point in space. The X-ray measurements were performed on polished cross-sections parallel to the building layers mounted in the goniometer with the scanning direction (SD) parallel to the conventional rolling direction (RD) as indicated on Fig. 1. Measurements on virgin powder were used to correct the measured pole figures and the calculated pole figures took into account the orthorhombic symmetry of the process. The MTM–FHM texture processing software and MTEX Software Toolbox [13] were used to calculate the pole figures, texture indices and normalized texture differences. Electron backscattered diffraction (EBSD) was performed on a TSL orientation imaging microscope system mounted on a Philips scanning electron microscope XL30, which is equipped with a tungsten gun. The step size was 0.4 μm on all the EBSD scans.

On all averaged values, a confidence interval of 95%, based on the variance σ_{n-1}, is used to indicate the spread.

3. Results

3.1. Microstructure

In Fig. 2, three cross-section views of sample A are given. Upon etching, the long scan vectors are revealed in the top and side view; the cross-sections of the melt pools become visible in the front view. It can be seen that the melt pools are half-cylindrical in shape. The size of the melt pools can be determined based on the cross-sections of the top melt pools in the front view. Based on pixel count, the melt pool height is determined to be 110 ± 10 μm (calculated based on microstructure pictures of all samples) and the width (based on the measured half-width) to be 170 ± 15 μm (for samples A and B) and 180 ± 30 μm (for samples D and E). The applied hatch spacing of 105 μm thus causes an overlap of 38–44% of the melt pool width between neighbouring scan tracks.

Due to the half-cylindrical shape of the melt pool and the partial remelting of previously deposited layers, the cross-section of melt pools from different layers can be seen in the top view. Note that due to variations in depth and shape of the melt pool, the melt pools are not always seen continuously. Near the edge of the part, melt pools produced in up to four different layers can be discerned. From this, one can observe that a steep and deep melt pool is formed at the start/end points of the scan tracks. It is believed here that heat is accumulated at these points of the scan paths and a keyhole melt pool is created. Since the keyhole equilibrium is very sensitive [14] and the transient character of the temperature evolution is at the

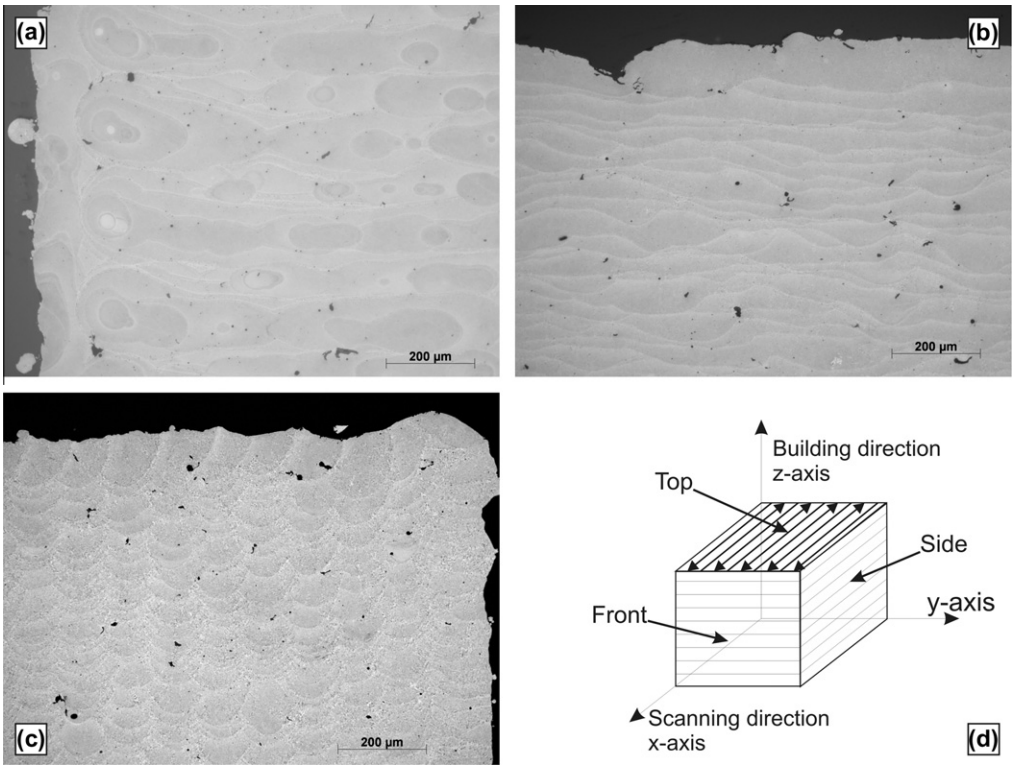

Fig. 2. Macrostructure of AlSi10Mg by SLM. In this figure, the macrostructure in the top (a), side (b) and front (c) view cross-sections of sample A is shown. Views are presented schematically in (d).

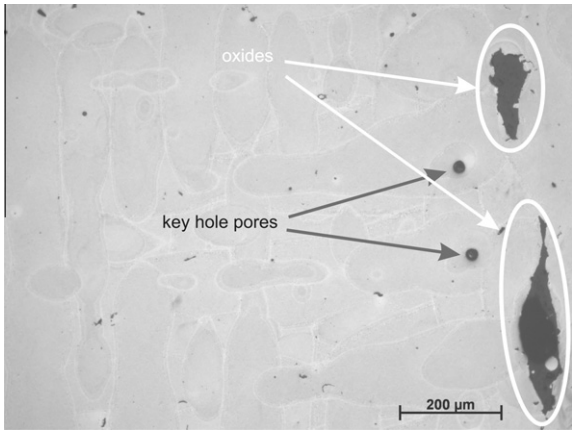

Fig. 3. Defects in AlSi10Mg SLM parts. Keyhole pores at the end of the scan track and oxide material in a top view micrograph of sample D etched by Keller's are indicated by respectively white and grey arrows.

start/end points, the keyhole becomes easily unstable and will collapse, thereby creating large pores. Those pores are shown in Fig. 3. Apart from these large pores, other pores and secondary oxide particles are observed in the SLM parts.

Although measures are taken to carry out the SLM process in an inert argon atmosphere, the atmosphere can still contain 0.1–0.3% residual oxygen and oxides may still be formed. The presence of Al oxides in the SLM products was also noted by Louvis et al. [6], who attributes the difficulty in producing dense aluminium parts with SLM mainly to the presence of these oxides. He concludes that the power of the laser should be high enough to break through the oxide layer formed on top of the deposited tracks. The parts in this study were produced at very high power (200 W instead of 50–100 W, which was used by Louvis et al. [6]). This ensured the breaking of the oxide phase on top of the substrate and nearly full dense parts could be produced. However, part of this oxide material is seen to be entrapped inside the SLM parts. As mentioned before, more details on the different types of porosity and secondary phase particles will not be discussed in further detail in this paper.

A closer look into the microstructure of sample B with the scanning electron microscope in Figs. 4 and 5 reveals the presence of a very fine cellular–dendritic solidification structure with a size smaller than 1 μm. The grey cellular features are primary Al and are decorated with white fibrous Si particles. Although this alloy can precipitate out Mg_2Si, the only phases that could be detected in the XRD patterns are the face centred cubic aluminium and the diamond like cubic silicon phase. Due to the fine dispersion of Si in the Al phase, the Vickers hardness of the as-built AlSi10Mg SLM parts is very high, namely 127 ± 3 Hv0.5. This hardness value is much higher (almost 30 Hv) than the hardness of a high pressure die casted (HPDC) AlSi10Mg in the as-cast condition (95–105 Hv) and almost as high as the HPDC AlSi10Mg in the aged condition (130–133 Hv) [15].

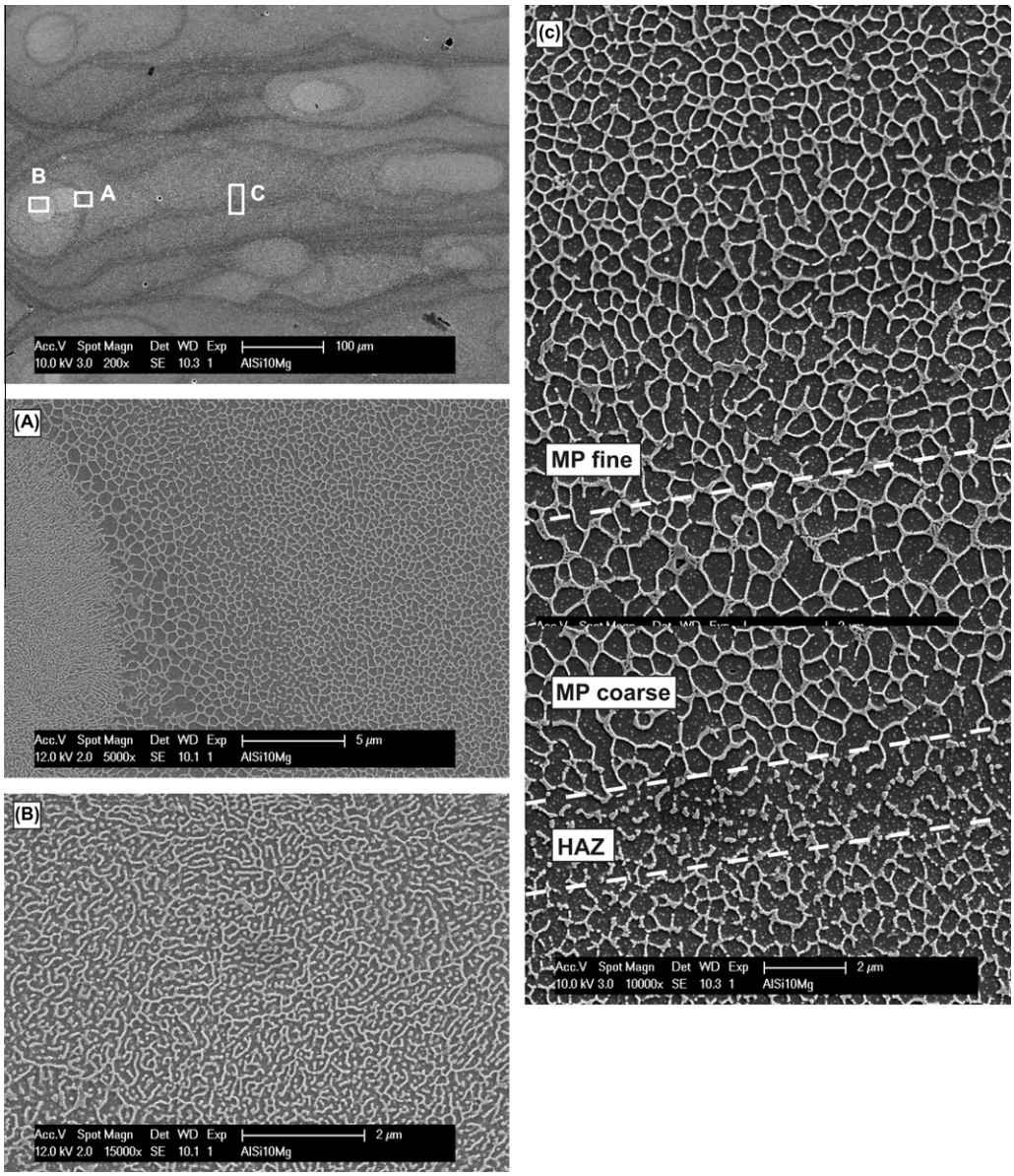

Fig. 4. Microstructure of an AlSi10 Mg SLM part in top view by SEM. Top view SEM micrographs of a sample produced with long bidirectional scanning tracks (sample B). The sample was etched with Keller's. The location of pictures A–C are indicated on the top left picture. In picture C, the melt pool zone with fine ("MP fine") and more coarse ("MP coarse") structure are indicated as well as the heat affected zone ("HAZ").

Across the melt pool, three different zones can be distinguished, as indicated in Figs. 4 and 5. The different zones are a fine ("MP fine") and a coarse ("MP coarse") cellular structure inside the melt pool and a heat affected zone ("HAZ") around the melt pool in the previously deposited layers.

Inside the melt pool cellular–dendrites grow towards the centre of the melt pool. This is seen from the transversal cross-section of the cells in the top view and the longitudinal cross-section in the front and side view in Figs. 4 and 5. The solidification mode is mainly cellular, but occasionally, some side branches can be seen. The fineness of the cells is not constant, but a transition from coarser cells (cell size of 0.7 μm) to finer cells (cell size of 0.4 μm) is seen at ~5 μm from the melt pool border (middle broken line in Figs. 4 and 5). Furthermore, it should be noted that the structure at the bottom of a keyhole, seen at location A in Fig. 4, is extremely fine. The cell size is smaller than 0.2 μm. The Al–Si eutectic is seen at some triple and quadruple points, mainly in the coarse MP structure.

Outside the melt pool, the intercellular network is broken by coarsening of the silicon phase into idiomorphic particles. This is caused by the increase in diffusion rate of the Si in the heat affected zone.

3.2. Texture

The directional solidification in the melt pool seen above is causing not only a morphological texture but a crystallographic texture as well. This was also indicated by the

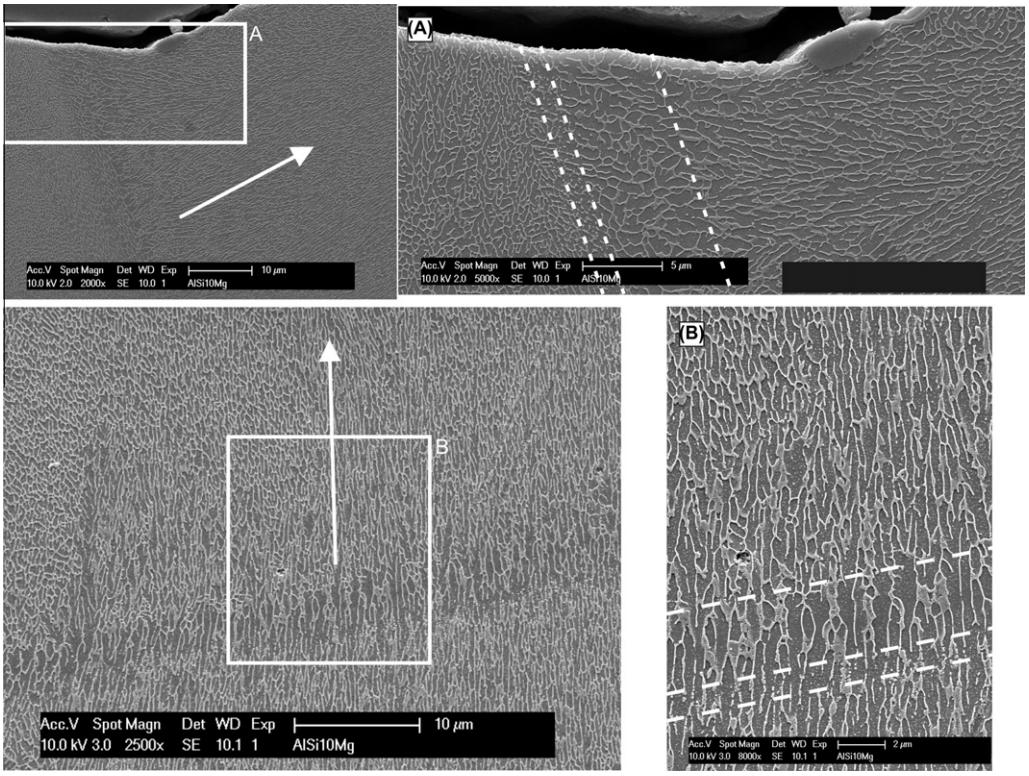

Fig. 5. Microstructure of a AlSi10Mg SLM part in front and side view by SEM. Front (top) and side view (bottom) SEM micrographs of a sample produced with long bidirectional scanning tracks (sample B). The graphs on the right are a magnification of the areas indicated by the white box. The sample was etched with Keller's. The white lines are indicating the different zones and the arrow is indicating the general dendrite orientation.

XRD patterns, in which the (200) peaks, and to a lesser extent the peaks corresponding to the (220) and (311) planes for the cubic aluminium phase, were more intense than the same peaks in for a reference material (JCPDS reference pattern 04-0787). Due to the moving heat source, the melt pool is not circular, but elongated. As a result, the scanning strategy is expected to have an influence on directionality of the solidification. Therefore, the texture resulting from different scanning strategies are compared here.

When a sample is scanned with long vectors and the scanning direction is kept the same for every layer, a strong ⟨100⟩ texture along the scanning direction and a weaker ⟨110⟩ texture along the building direction arise. This can be seen from the inverse pole figure parallel to the scanning direction shown in Fig. 6a. The low intensities in the remaining inverse pole figures suggest the presence of a fibre texture. However, this fibre is not complete, as can be seen from the (100) pole figure. The high diffraction peak intensities of the ⟨100⟩ directions only vary between −70° and +70° to the building direction with a maximum intensity from −41° to +41°. The overall texture intensity is given by the texture index:

$$\text{Texture index} = TI = \int_{eulerspace} (f(g))^2 dg \qquad (1)$$

where f is the orientation distribution function as a function of the Euler space coordinates g. This was calculated to be 1.974. For isotropic materials, this texture index is equal to unity [16].

To investigate the effect of the unidirectional vs. bidirectional methods of scanning, the texture of sample B was also measured. The texture for sample B appeared to be similar to that of sample A. The normalized texture difference between sample A and B with reference to sample A was calculated according to the following equation:

$$\text{Norm. text. diff.} = \frac{\int_{eulerspace} (f_A(g) - f_B(g))^2 dg}{\int_{eulerspace} (f_A(g))^2 dg} \qquad (2)$$

where $f_A(g)$ and and $f_B(g)$ are, respectively, the orientation distribution functions of samples A and B as a function of the Euler space coordinates g. The normalized texture difference amounts only to 0.64%, and therefore it can be concluded that the method of scanning does not affect the crystallographic texture of the SLM parts.

Viewing aluminium samples with polarized light after anodizing with Barker's reagent is known to reveal the different grain orientations. In Fig. 7a and b, the optical polarized light graphs of the front and side view of sample A are shown. Both show the grain structure of the last molten melt pools at the top of the part. In the front view of the melt pools in Fig. 7a, it is seen that grains are growing perpendicular to the melt pool border towards the centre of the melt pool. At the top of the melt pool, smaller equiaxed grains are observed. In the side view in Fig. 7b, some grains

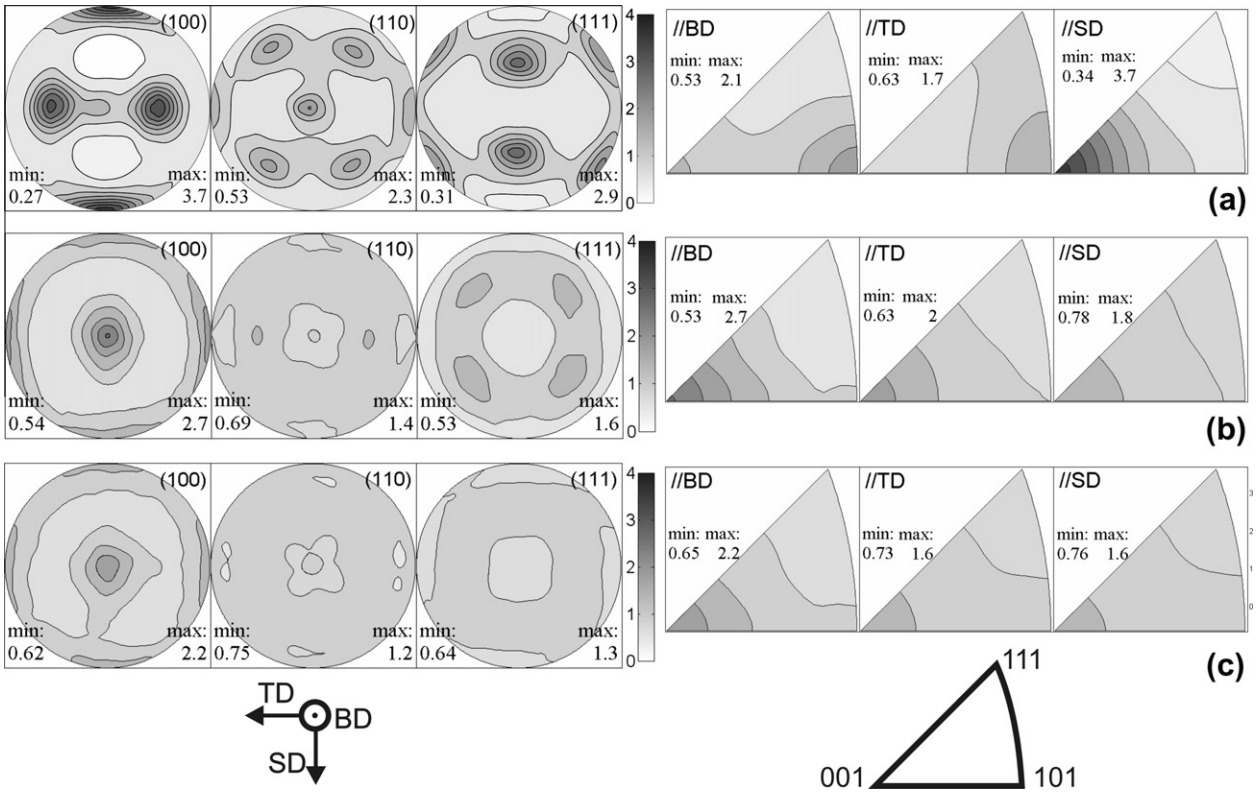

Fig. 6. Pole figures and inverse pole figures for AlSi10Mg SLM parts produced using different scanning strategies. The (1 0 0), (1 1 0) and (1 1 1) pole figures (left) and inverse pole figures (right) parallel to the building direction (BD), scanning direction (SD) and the transverse direction (TD) are given. Figs are shown for a sample produced with: unidirectional long scanning vectors (sample A) (a); bidirectional long scanning vectors rotated 90° (sample C) (b) and island scanning without shift (sample D) (c). Furthermore, the orientation of the specimen coordinate system is shown and the relative intensity of the diffraction peaks compared to an isotropic powder material reference sample is indicated by the grey scale.

have grown across the melt pool borders. In this side view, smaller equiaxed grains can also be seen at the top of the melt pools. Due to the overlap between neighbouring tracks and the remelting of previous layers, only a part of the solidified melt pool will remain. This results in alternating bands of ~50 μm wide parallel to the scanning direction with different grain and crystallographic orientations.

When the scanning direction is rotated by 90° every layer, as was mimicked with sample C, the overall crystallographic texture is significantly reduced, as illustrated in the pole figures in Fig. 6b. The texture index is lowered from 1.974 for sample A and 1.982 for sample B to 1.266 for sample C. This is a reduction of 35%. By mimicking a rotation of the scanning direction of 90° between the layers, the ⟨1 0 0⟩ fibre texture along the scanning direction is significantly lowered and is replaced by a weaker ⟨1 0 0⟩ cube texture along the building direction and to a lesser extent along the scanning directions, both the first scan and the second scan.

In Fig. 7c, both the transversal (circular in shape) as well as the longitudinal (elongated) cross-sections of the melt pools are shown. The depth and width of the second scanned pools are measured to be respectively 70 μm and 180 μm (based on the transversal cross-sections of the melt pools at the top). The second scanned pools are thus 40 μm less deep than the perpendicular first scanned melt pools. Because of this difference in height, part of the first scanned and solidified material remains and contributes to a reduction in the texture by a larger spread in grain and crystal orientations. However, it is seen from the ⟨1 0 0⟩ pole figure in Fig. 6b that the high intensity zone is elongated in the SD direction, which implies still a higher contribution of the first formed melt pool structure (due to the difference in melt pool size) than of the second scanned pools.

Reducing the texture by varying the scanning direction can also be done by rotating the scanning direction within one layer. This is done by island scanning, in which the scanning direction is rotated 90° between neighbouring islands (sample D). The recalculated pole figures are shown in Fig. 6c. Again, only a weak ⟨1 0 0⟩ cube texture along the building direction is obtained. The texture index is lowered to 1.127.

Because of the more equal volume percentage of grains resulting from scanning in each direction, a slightly more isotropic structure is obtained in sample D than in sample C. However, the normalized texture difference between samples D and C with reference to sample C is only 3.5%.

Because aligned pores can be formed at the island borders, the position of the islands between each layer is shifted for 1 mm (sample E). Since the texture is mainly dependent on the local heat fluxes and to a lesser extent

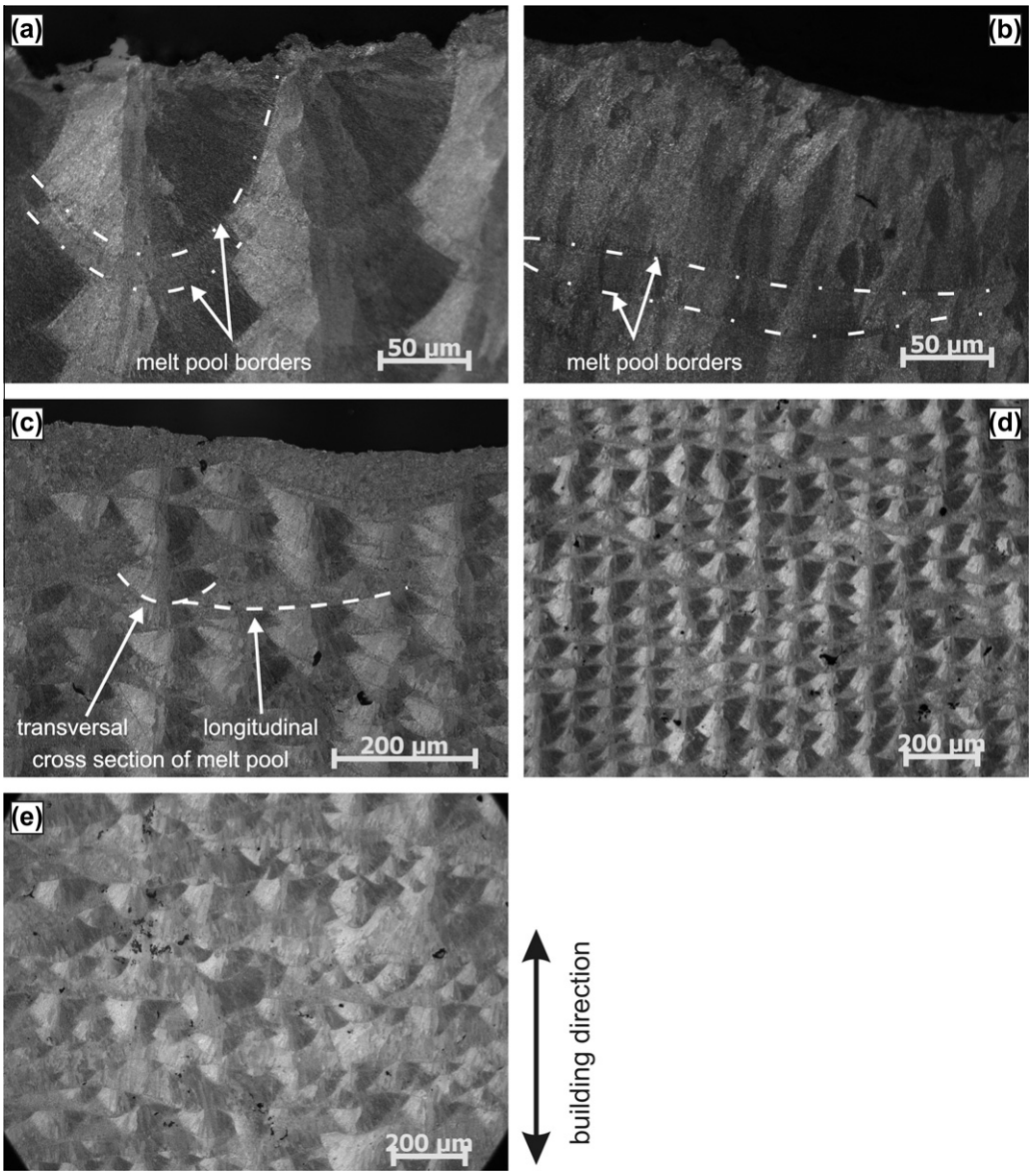

Fig. 7. Grain structure of AlSi10Mg SLM part revealed by polarized light. Polarized light optical micrographs of the (a) front view and (b) side view cross-section of the part produced with unidirectional scan vectors (sample A); (c) micrograph of the view perpendicular to the first scanned vectors and parallel to the second scanned vectors (sample C); micrographs from parts produced with islands (d) without (sample D) and (e) with 1 mm shift of the island borders between the successive layers (sample E) are shown.

on the substrate crystallography, the shift is seen to have no significant influence on the texture. The normalized texture difference between sample E (with shift) and sample D (without shift) with reference to sample D is only 1%.

The grain structure for island scanning with and without shift of the islands position is illustrated in Fig. 7d and e. Although the global texture is similar, it can be seen that the local texture is still different. When the islands are scanned on top of each other, the parallel alternating layers of equal grain and crystal orientation are still present, only this time intersected by the perpendicularly scanned tracks. When shifting the island positions, this local texture is lost.

Only for sample E were texture measurements at different heights along the sample performed. The texture was measured at heights of 0.25, 8.0 and 9.9 mm and the normalized texture differences of the second and third slice compared to the first one were calculated to be less than 0.3%. This suggests that the texture is not varying over the height of the sample and that no competitive growth mechanism is present on a large scale (i.e. not outside the melt pool).

Fig. 8 gives the EBSD graph of the front and top view of sample B. The front view shows the grain structure of several melt pools scanned perpendicular to this section. The different melt pools can be distinguished because the elongated grains always grow towards the centre of the melt pool and epitaxial growth only occurs at specific places. At the centreline of the melt pool, grains grow epitaxially; whereas away from the centreline, small newly nucleated grains can be observed. Amongst those newly nucleated grains,

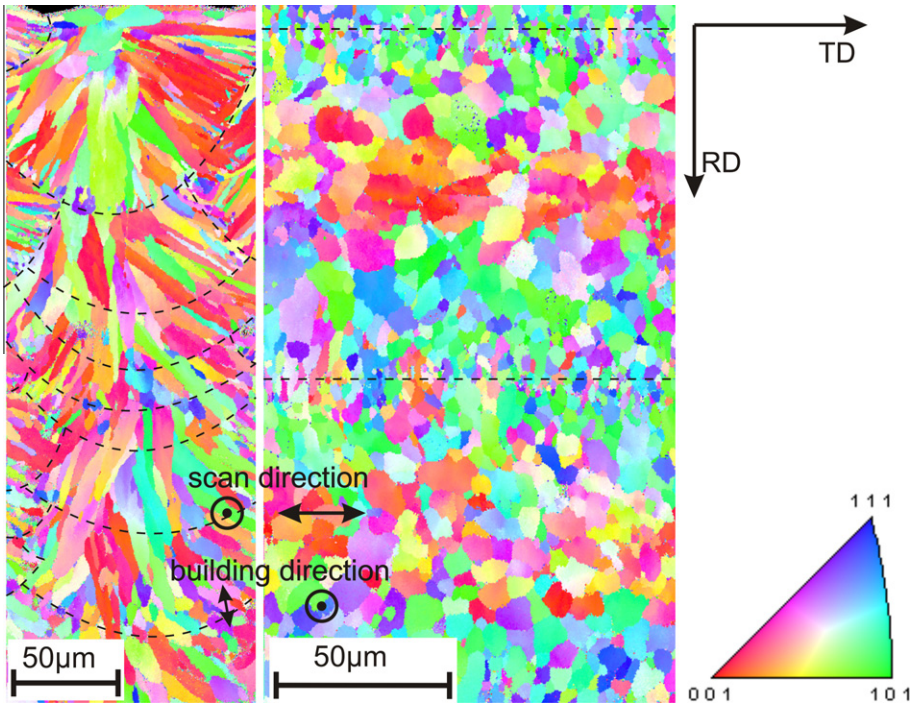

Fig. 8. EBSD orientation maps in two perpendicular views for an AlSi10Mg SLM part. EBSD maps of the front view (left) and top view (middle) of sample B. The scanning and building direction is indicated by the black arrows on the pictures and some of the melt pool borders are pointed out by the dashed lines. The specimen coordination system and the crystal orientation–colour relation map referenced to the direction perpendicular to TD and RD are shown at the right.

competitive growth has taken place. Only a few orientations can grow further towards the melt pool centre. Furthermore, at the top layer of the part (seen at the top of the front view picture), equiaxed grains have formed at the top of the melt pool. However, for each layer, the top part of the solidified melt pool of the previous layer will be remelted when scanning the next layer. The amount of remelting equals the melt pool height of ~100 μm minus the layer thickness of 30 μm, which is 70 μm. As a result, the equiaxed grains from the top of the melt pool are remelted and will disappear from the structure. Only those equiaxed grains from the last scanned layer of the part will last.

In the top view, bands parallel to the scanning direction are visible. In a small region around the melt pool borders, small grains (<3 μm) of different colours are present. Between the border and the centreline, the grains are larger (~6 μm) and have a green–blue colour. Finally, large (~12 μm) reddish grains are present around the centreline of the melt pool. When speaking in terms of orientations, small grains with random orientations are present at the melt pool border. At the centreline, grains have their ⟨0 0 1⟩ orientation parallel to the building direction and in between, the grain directions between ⟨1 1 0⟩ and ⟨1 1 1⟩ are oriented along the building direction.

4. Discussion

The distinctive process of adding material track after track and layer after layer together with the fast and directional cooling rates during selective laser melting creates a unique microstructure in the products. The microstructure inside a scan track is dependent on the value and direction of the thermal gradients at the border of the moving melt pool and is repeated in a similar way for every scan track. The macrostructure is determined by the way in which the different individual tracks are combined. In other words, it is defined by the method of scanning the cross-section of a certain slice of the product. This is also referred to as the scanning strategy.

The mode of solidification and feature fineness is dependent on the thermal gradient G and the growth rate R [17]. The thermal gradient G is the difference in temperature over a certain distance $\mathrm{d}T/\mathrm{d}x$ and varies over the time and place inside the melt pool. The growth rate R depends on the speed of the moving source v and the angle between the direction of the moving source and the growth direction of the solidifying material θ. R is equal to the product of v and the cosine of θ when steady state conditions are assumed (as is done here for simplicity). The G over R ratio determines the stability of the solidification front and hence the resulting solidification mode. From high to low ratios consecutively a planar, cellular, columnar dendritic and equiaxed dendritic structure is expected. The multiplication of G and R determines the fineness of the structure; the higher the product, the finer the structure. The product of G and R gives the cooling rate and therefore is a measure for the diffusion length of the solutes of the forming solid phases during solidification and thus the fineness of the structure.

An estimation of the highest occurring temperature gradient in space was done using the model developed by Verhaeghe et al. [18] but adapted for this material and these process parameters. This shows that thermal gradients as high as in the order of 10^6 K m^{-1} can occur. This explains the very small cell size observed in these AlSi10Mg SLM parts.

Due to the movement of the heat source, the thermal gradients and growth rates vary over the melt pool. They are the highest at the centreline of the melt pool and decrease when going towards the border of the scan track. The growth rate even reaches zero at the melt pool border where the laser movement direction is perpendicular to the heat transfer. As a result of the changing G and R, also the mode of solidification and the fineness will vary. However, since G and R are varying qualitatively in a similar way, no significant change in solidification mode is expected. In the micrographs shown above, only cellular solidification with an occasional side branch is observed. Furthermore, the equiaxed grains at the top of the melt pool are expected to result from surface nucleation. The product of G and R, which determines the fineness of the microstructure, however, will vary significantly. This was also evident in the micrographs in Figs. 4 and 5, where a change in cell size from 0.7 μm to less than 0.4 μm is seen along the melt pool.

When the cellular solidification mode is active, cubic materials are known to preferentially grow the cells along the ⟨1 0 0⟩ crystal direction [17]. Since a relatively small melt pool is created on top of a large already consolidated block of material, the heat flows away radially and grains grow towards the centre of the melt pool. This creates a morphological as well as crystallographic texture in the parts. If we would consider only a single track, a ⟨1 0 0⟩ fibre and more precisely even a half-cylindrical ⟨1 0 0⟩ texture around the scanning direction is expected. At places where the ⟨1 0 0⟩ direction of the substrate is along the heat flow direction, i.e. around the centreline, grains grow epitaxially. Near the border of the melt pool, new nuclei are formed and competitive growth occurs. During SLM, however, the above and aside neighbouring tracks cause partial remelting of the solidified track. As a result, the ⟨1 0 0⟩ fibre around the scanning direction is not complete but reduced from −70° to +70° with maxima at +and −40° (as seen in the 100 pole figure in Fig. 6a). This was also verified by measuring the highest angle of the grains towards the building direction. It was found that the highest angle varies between 30° and 70°. Furthermore, due to the partial remelting the morphological texture is increased since the majority of the elongated grains will now be oriented along the building direction. It is interesting to note that the extent of the morphological and crystal texture could be adjusted by varying the hatch spacing and/or the layer thickness since these parameters directly determine the amount of partial remelting of the neighbouring tracks. A smaller layer thickness and/or hatch spacing would intensify the morphological and the crystal texture. The adjustment of the texture by varying these parameters, however, is limited by the process window to obtain sound parts [7].

The texture, however, can also be influenced by varying the paths of the laser. The uni- or bidirectional way of scanning has no influence on the created texture, as opposed to the findings for laser deposition of another Al–Si alloy [11]. The reason for this difference in behaviour is the different ratio of melt pool size compared to the part dimensions. In laser deposition, single beads are placed on top of each other while in SLM melt pools of ~175 μm are created on a part of 1 cm^2 cross-section. As a result, the heat is directed more vertically in SLM while in laser deposition, it is slanted towards laser movement.

The direction of scanning, however, has a significant influence in SLM. When the scanning direction is rotated over 90°, the texture is significantly reduced and a weak cubic texture along the building direction arises. Furthermore, no difference is observed between rotating the scanning directions between consecutive layers, or rotating the direction within one layer by using island scanning. Using other rotations than 90°, e.g. 60° or 45°, is expected to be able to lower the texture even further and make the SLM product more isotropic. Unfortunately, this could not be checked since the Concept Laser M1 does not allow other rotations than 90°.

5. Conclusion

The unique process conditions during SLM causes a very fine microstructure consisting of submicron cells growing along the ⟨1 0 0⟩ crystal direction towards the centre of the melt pool. The face centred cubic aluminium cells are decorated by a diamond-like silicon phase. This fine distribution leads to a high hardness of the SLM parts, i.e. 127 ± 3 Hv0.5. Due to the moving heat source, the thermal gradients and growth rate vary over the melt pool and the fineness of the cells is seen to change from below 0.7 μm at the melt pool border to 0.4 μm in the middle of the scan track. This change in cell size makes it possible to distinguish the melt pool tracks at the macroscale.

Due to the partial remelting of previously scanned neighbouring tracks, a morphological as well as crystallographic texture arise. At the centreline of the tracks, elongated grains grow along the building direction. Depending on the applied scanning strategy, a strong partial ⟨1 0 0⟩ fibre along the scanning direction or a weak cubic texture preferentially around the building direction is formed. The first one is present when no rotation of scanning direction is applied; the latter one when 90° rotation in the layer or between the layers is applied.

Although there is partial remelting of the substrate and consequently the absence of a nucleation energy barrier, epitaxial growth occurs only if the heat flow is directed favourably to the ⟨1 0 0⟩ crystal direction of the substrate. If not, new nuclei will be formed and competitive growth will favour the grains with their ⟨1 0 0⟩ along the heat flow direction. This competitive growth plays only over the

height of one melt pool. Therefore, the texture of the SLM parts is constant over the height of the part.

This study shows that AlSi10Mg parts with an extremely fine microstructure and hence a high hardness can be made by SLM. Furthermore, by also considering the macrostructure, it is shown that a morphological and crystallographic texture is present and that a more anisotropic or isotropic part can be obtained by choosing the applied scanning strategy.

Acknowledgements

This research was funded by a PhD grant from the Agency for Innovation by Science and Technology (IWT). Partial financial support from GOA/10/12 is also appreciated. The authors would like to thank Ling Qin for his help with the EBSD analyses.

References

[1] Wong M, Tsopanos S, Sutcliffe CJ, Owen I. Rapid Prototyping J 2007;13(5):291–7.
[2] Kruth JP, Levy GN, Klocke F, Childs THC. Ann CIRP 2007;56(2):730–59.
[3] Kearney AL. ASM handbook, vol. 2. ASM International: Materials Park, OH; 1990.
[4] ASM International. ASM handbook, vol. 4. Materials Park, OH: ASM International; 1991.
[5] Buchbinder D, Schleifenbaum H, Heidrich S, Meiners W, Bültmann J. Phys Procedia 2011;12:271–8.
[6] Louvis E, Fox P, Sutcliffe CJ. J Mater Process Technol 2011;211:275–84.
[7] Kempen K, Thijs L, Yasa E, Badrossamay M, Verheecke W, Kruth J. In: Paper presented at the solid freeform symposium (SFF2011), Austin, Texas; 2011.
[8] Brandl E, Heckenberger U, Holzinger V, Buchbinder D. Mater Des 2012;34:159–69.
[9] Watkins KG, McMahon MA, Steen WM. Mater Sci Eng A 1997;231:55–61.
[10] Wong TT, Liang GY, Tang CY. J Mater Process Technol 1997;66:172–8.
[11] Dinda GP, Dasgupta AK, Mazumder J. Surf Coat Technol 2012;206:2152–60.
[12] Concept Laser GmbH/M1. Web-based data. Concept Laser GmbH Co., Germany. <http://www.concept-laser.de/> [as on 15.07.11].
[13] Bachmann F, Hielscher R, Schaeben H. Solid State Phenom 2010;160:63–8.
[14] Ion JC. Laser processing of engineering materials: principles, procedure and industrial application. Oxford: Butterworth-Heinemann; 2005.
[15] Lumley R. Technical data sheets for heat treated aluminium high pressure die castings. CSIRO Light Metals Flagship. <http://csiro.au/science/ps1f1.html>.
[16] Kocks UF, Tomé CN, Wenk HR. Texture and anisotropy. Cambridge: Cambridge University Press; 1998.
[17] Glicksman ME. Principles of solidification. New York: Springer; 2011.
[18] Verhaeghe F, Craeghs T, Heulens J, Pandelaers L. Acta Mater 2009;57(20):6006–12.